Intrinsic relaxation rates of polarized Cs vapor in miniaturized cells

Theo Scholtes · Stefan Woetzel · Rob IJsselsteijn ·
Volkmar Schultze · Hans-Georg Meyer

Abstract The intrinsic relaxation rates of the vector magnetization of cesium vapor enclosed in microfabricated atomic magnetometer cells are investigated. Two methods—the optically detected magnetic resonance and the ground-state Hanle effect—are used to carry out automated measurements in dependence on cell temperature and nitrogen buffer gas pressure. The experimental results are compared with expected contributions of the different relaxation processes and in this way allow the discrimination between them to help further optimization of cell design. The methods are compared in terms of basic features, data quality, and practical applicability.

1 Introduction

Optical magnetometry [1, 2], although known and applied for more than half a century now [3–5], has seen great advancements over the last years [6–9]. Nevertheless—thanks to their convenience in use—the basic part of every practical optical magnetometer device remains the same: a cell containing spin-polarized thermal alkali metal vapor as the sensors' active medium. To maintain the spin polarization of the optically pumped [10] atoms inside the cell as long as possible, one has to take steps against the effect of depolarizing wall collisions. To this end, two different strategies in cell design are commonly pursued. One way is to use cell coatings to prevent depolarization of the atoms upon wall collisions. While invented in the early days of

T. Scholtes (✉) · S. Woetzel · R. IJsselsteijn · V. Schultze ·
H.-G. Meyer
Leibniz Institute of Photonic Technology, Albert-Einstein-
Strasse 9, 07745 Jena, Germany
e-mail: theo.scholtes@ipht-jena.de

optical magnetometry already [11, 12], intensive study is still ongoing and improvement of their properties for use in glass-blown vapor cells is still a hot topic [13–15].

The other way known for a similarly long period of time (cf. [10] and refs. therein)—and investigated here—is the introduction of buffer gases like helium or nitrogen into the cell to hinder the atoms from reaching the cell walls. Since the buffer gas particles collide with the alkali atoms as well and consequently give rise to an additional polarization–relaxing process, the optimal buffer gas pressure, and species, leading to the lowest total depolarization rate is of high practical interest for optimized cell performance. Besides these two processes the third relaxation process one has to consider is alkali–alkali collisions, where total-spin-conserving spin-exchange and less frequent spin-nonconserving spin-destruction collisions are distinguished [16]. Hence, the counterplay of wall and buffer gas relaxation determines the minimal magnetic resonance line-width achievable as long as the impact of alkali–alkali collisions is either negligible (i.e., at low cell temperatures) or largely suppressed [17–20]. The four processes described above depend only on cell design and temperature and are thus termed to be "intrinsic." Investigation of these processes allows for a measure of the vapor cell's performance.

The magnetic linewidth of most practical implementations of optical magnetometers is not only made up of the intrinsic relaxation processes, but suffers from additional contributions due to power broadening of the magnetic resonance. The interaction of pump and/or probe light with the alkali atoms as well as the action of a radio frequency (rf) field, as used with the M_x-configuration [21], act as relaxation processes (termed "operational" here) on their own. To infer the intrinsic relaxation rates, one has to eliminate these operational contributions, for example, by

extrapolation to vanishing laser power as performed in this work.

The intrinsic longitudinal and transverse relaxation rates γ_1 and γ_2 have been determined using the method of optically detected magnetic resonance (ODMR) in a M_x-setup [7, 13] and using measurements based on the ground-state Hanle effect (GSHE) as described recently for paraffin-coated vacuum cesium cells at room temperature [22, 23].

Contrastingly, in this paper, we use miniaturized cell structures, which are fabricated based on silicon wafer microstructuring and bonding technology. [24]. These cells—unlike the paraffin-coated versions investigated before—are intended for operation at up to 150°C. Furthermore, the use of MEMS technologies enables the production of cell structures of identical geometry and the precise introduction of the desired nitrogen amount. The ability to control the cell temperature and buffer gas pressure over a large range allows us to investigate the dependence of the intrinsic relaxation rates on these parameters and thus facilitates the discrimination of the intrinsic contributions of wall, buffer gas, and alkali–alkali collision rates.

Besides supporting the further optimization of our cell design, the discrimination of the relaxation contributions is motivated by the desire for a deeper understanding of the processes responsible for the huge gain in sensitivity observed with the "light-narrowed" (LN) magnetometer presented recently [25, 26], i.e., to what extent the spin-exchange relaxation contribution can actually be suppressed.

After a short description of the two methods, the intrinsic relaxation processes and the experimental setup, the results of the measurements using six cells of identical geometry filled with different number densities of nitrogen are presented and discussed.

2 Methods

2.1 Optically detected magnetic resonance (ODMR)

This method is based on the M_x-setup [21]: a magnetic field B_0, tilted at 45° relative to the laser propagation direction, causes Larmor precession of the vector magnetization that is created by circularly polarized optical pumping. Application of an additional magnetic field B_1 oscillating at a frequency ω near the Larmor frequency of the atoms $\omega_L = \gamma_F B_0$, where $\gamma_F \simeq 2\pi \cdot 3.5$ Hz/nT is the Cs ground-state gyromagnetic ratio, allows the magnetic resonance to be detected in the modulation amplitude and phase of the cell-transmitted light. Recording the separate in-phase and quadrature components of the resonance as a function of the detuning $\delta = \omega - \omega_L$ by lock-in detection at the first

harmonic, leads to Lorentzian-shaped signals [13]. Unfortunately, fitting these curves for the determination of γ_1 and γ_2 suffers of strong parameter correlations between the two rates and the unknown experimental signal amplitude calibration constant. For that reason, we restrict our interest to the determination of γ_2, as this is the relevant parameter for determining a magnetometers' sensitivity. The value of γ_2 can be inferred by a fit to the phase signal of the lock-in, which is independent of the overall signal amplitude, B_1 field calibration and is governed only by γ_2 according to

$$P_{\text{phase}} = -\arctan\left(\frac{\delta}{\gamma_2}\right). \tag{1}$$

The phase signal is not prone to B_1-power broadening [27], however γ_2 is increased by the nonzero laser power that must be used. So measurements are taken at several different laser powers and subsequently extrapolated to zero laser power. In this way, the intrinsic transverse relaxation rate γ_{20} is inferred.

2.2 Ground-state Hanle effect (GSHE)

The Hanle effect, originally observed by and named after W. Hanle, gives rise to changes in polarization of resonance fluorescence in dependence on a static magnetic field [28]. It originates from precession and relaxation of spin polarization in the atomic excited state and can be used to measure either lifetime or magnetic moment of excited states [29]. The resonances appear centered at zero magnetic field ($B = 0$) where the degeneracy of the magnetic sublevels of the atomic spin state leads to the creation of coherences among them [30]. These effects may also emerge in the atomic ground states as firstly observed in the 1960s by researchers in France, who monitored the transmitted intensity of circularly polarized light in dependence on the strength of a transverse magnetic field [31, 32]. The authors explained their observations in virtue of the GSHE. The GSHE using circularly polarized light has been explored by a number of groups in the past (see, e.g., [32–37]), but a full theoretic treatment ready for application has been worked out only very recently by Castagna and Weis [22, 23]. The authors also give an extended historic survey and classification of the GSHE.

We investigated the described formalism as a competing approach to the simultaneous determination of the relaxation rates γ_2 and γ_1, for that purpose, we decided to constrain our experiments to the use of the longitudinal Hanle effect (LHE) as it was found by Castagna and Weis to offer a better data quality and less problematic fit parameter correlations than the measurements based on the transverse Hanle effect (THE). For the LHE, a magnetic field $B_\perp \equiv B_x$, transverse to laser direction z, acts as parameter field that is varied in a stepwise manner, while for every

transverse field value the transmitted light power is recorded when the longitudinal field is swept over $B_\parallel \equiv B_z = 0$. The amplitudes A and widths W of the resulting Lorentzian resonances depend on the Larmor frequency of an applied transverse field $\omega_x = \gamma_F B_x$ according to

$$A(\omega_x) = A_0 \left[1 - \frac{\gamma_1 \gamma_2}{(\omega_x + \delta\omega_x)^2 + \delta\omega_y^2 + \gamma_1 \gamma_2} \right] \quad (2)$$

and

$$W(\omega_x) = \sqrt{\frac{\gamma_2}{\gamma_1}(\omega_x + \delta\omega_x)^2 + \gamma_2^2 + \frac{\gamma_2}{\gamma_1}\delta\omega_y^2}, \quad (3)$$

where $\delta\omega_x$ and $\delta\omega_y$ are unknown residual transverse field components that might be apparent [22, 23]. To avoid parameter correlations, the fitting functions are parameterized as

$$A_{\text{fit}}(\omega_x) = P1 \left[1 - \frac{P2}{(\omega_x + P3)^2 + P4^2} \right] \quad (4)$$

and

$$W_{\text{fit}}(\omega_x) = \sqrt{P5(\omega_x + P6)^2 + P7^2}, \quad (5)$$

where the fit parameters $P2 = \gamma_1 \gamma_2$ and $P5 = \frac{\gamma_2}{\gamma_1}$ then allow the determination of the individual relaxation rates. In analogy to the ODMR method, the rates depend on the laser power used, and so, the determination of intrinsic γ_{10} (γ_{20}) requires an extrapolating fit with several γ_1 (γ_2) measured at different small laser powers. The dependence on laser power is found to be linear only in a narrow range of low laser powers, while for higher powers contributions due to creation of spin alignment may emerge. To account for this, we used (phenomenological) second-order polynomials for extrapolation as successfully demonstrated by Castagna and Weis.

2.3 Intrinsic relaxation processes

The discrimination of the relaxation mechanism contributions playing a role requires modeling each single process. As adapted from [38], the wall relaxation rate

$$R_{\text{WD}} = \left[\left(\frac{\pi}{d} \right)^2 + \left(\frac{2.405}{r} \right)^2 \right] \frac{D_{0,\text{Cs}-\text{N}_2}}{\eta} \sqrt{\frac{T}{273.15\,\text{K}}} \quad (6)$$

depends on the thickness d and radius r of the cylindrical cell, the cell temperature T and the diffusion constant of cesium atoms in nitrogen $D_{0,\text{Cs}-\text{N}_2}$ (given at 1 amg and 273 K). η is the nitrogen number density in multiples of one amagat n_0. The effect of buffer gas collisions is described by

$$R_{\text{BG}} = \eta n_0 \sigma_{\text{Cs}-\text{N}_2} \bar{v}_{\text{Cs}-\text{N}_2}. \quad (7)$$

where $\sigma_{\text{Cs}-\text{N}_2}$ denotes the depolarizing cross section of cesium in nitrogen and $\bar{v}_{\text{Cs}-\text{N}_2}$ the relative thermal velocity between the two species. Spin-exchange collisions with other cesium atoms lead to a relaxation rate of

$$R_{\text{SE}} = q_{\text{SE}} n_{\text{Cs}} \sigma_{\text{SE}} \bar{v}_{\text{rel}} \quad (8)$$

with $q_{\text{SE}} = \frac{7}{32}$ being the spin-exchange-broadening factor as used in [39], n_{Cs} the Cs vapor density that strongly increases with T, σ_{SE} the spin-exchange cross section and $\bar{v}_{\text{rel}}$ the relative thermal velocity of the Cs atoms. In a very low static magnetic field, the relaxation due to spin-exchange collisions was found to vanish [17, 18]. More precisely, the spin-exchange relaxation is absent if the Larmor frequency ω_L in the external static magnetic field is much less than the spin-exchange rate of the atoms. This regime was termed "SERF" (spin-exchange relaxation free) later on and used for the most sensitive implementations of optical magnetometers to date [9, 19, 20]. As the GSHE measurements are carried out near zero magnetic field, one should be prepared to observe this effect that consequently leads to the equality of the intrinsic rates γ_{10} and γ_{20} (cf. 6 and 7), if the SERF condition is fully met. However, as the magnetic field is swept around zero to record the GSHE resonances, we may not assume the intrinsic rates to be equal a priori, but instead to see a dependence of $\frac{\gamma_{20}}{\gamma_{10}}$ on the actual spin-exchange rate, i.e., on cell temperature T.

The rate equation of spin destruction due to collisions with other cesium atoms is similar to that of spin exchange, but the cross section of that process σ_{SD} is two orders of magnitude smaller:

$$R_{\text{SD}} = q n_{\text{Cs}} \sigma_{\text{SD}} \bar{v}_{\text{rel}} \quad (9)$$

Additionally, R_{SD} is diminished further by the nuclear slowing-down factor q (we set $q = \frac{1}{22}$ as we work at low spin polarization), which accounts for the possible repolarization of the electron spin by the polarized nucleus [40]. In contrast to spin-exchange collisions, spin-destruction interactions do not preserve the total spin of the ensemble of alkali atoms. Spin destruction becomes notable only at very high cell temperatures and when the impact of spin-exchange collisions is absent.

The overall intrinsic relaxation rates γ_{10} and γ_{20} that can be determined experimentally are made up of the summarized impact of the depolarization mechanisms according to

$$\gamma_{10} = R_{\text{WD}} + R_{\text{BG}} + R_{\text{SD}} \quad (10)$$

and

$$\gamma_{20} = R_{\text{WD}} + R_{\text{BG}} + R_{\text{SD}} + R_{\text{SE}}. \quad (11)$$

Using (6–9) with all the experimentally determined parameters nicely collected in [39], the overall intrinsic

rates (10) and (11) can be calculated without any free parameters.

3 Experimental setup

The experimental setup shown in Fig. 1 is only slightly modified from the one described more in detail in [41]. We investigate six cell array assemblies of identical geometry, and in each case, one of two measurement cells (4 mm in diameter and thickness) sharing a common Cs metal reservoir cavity is used (see inset of Fig. 1). The cell structures are implemented in a thick silicon wafer by ultrasonic milling and enclosed by bonded glass plates on both sides, after a solution of cesium azide has been pipetted to the reservoir chamber [24]. Before finally sealing the assembly, a well-defined nitrogen pressure is set inside the bonder recipient to establish a buffer gas pressure offset for the cells, a procedure known as "backfilling" [8]. In the subsequent decomposition of cesium azide into pure cesium metal and gaseous nitrogen by UV photolysis, an additional rise in buffer gas pressure takes place that can be controlled by the UV light dose. The final nitrogen number density captured inside the cavity is determined measuring the shift of the $D1$ absorption lines compared with a vacuum reference cell using data from [42].

For all measurements presented here, the narrow-band distributed feedback (DFB) laser light is circularly polarized and tuned to the hyperfine transition $F = 4 \rightarrow F' = 3$ of the Cs D_1 line ($\lambda = 894.6$ nm). As this transition shifts (and broadens) with increasing buffer gas pressure, an actively temperature-stabilized Fabry-Perot Interferometer (FPI) was implemented to lock the laser frequency. The cavity length of the FPI can be tuned conveniently by a dc voltage supplied to the piezo driver behind one of the mirrors. In this way, the FPI transmission peaks can be placed freely at the desired locking position on the absorption profile of the cell under investigation. The laser power in front of the fully-illuminated vapor cell is automatically controlled by a pair of rotatable linear polarizers. The silicon wafer of the cell array is heated conveniently by (far) off-resonant ($\lambda = 808$ nm) fiber-coupled laser radiation. The cell array temperature is monitored by a nonmagnetic fiber-optical sensor, whose tip is embedded into an ultrasonically drilled hole in the silicon wafer for optimized thermal contact. Coils on printed circuit boards are attached to both sides of the cell assembly to supply the B_1 field for the ODMR measurements. Pairs of Helmholtz coils produce magnetic fields in parallel (longitudinal) and perpendicular (transverse) to the laser direction for the GSHE method and a static 5 μT magnetic field at 45° relative to the laser axis for ODMR measurements. The coil current, for the sweeps of the longitudinal magnetic field, is produced by the amplified DAC voltage across a series resistor (1 kΩ). By comparing measurements with and without purposely applied additional magnetic field gradients, relaxation due to magnetic field gradients across the cell volume was checked to be negligible. The power of the cell-transmitted laser light is detected by a photo diode and amplified by a transimpedance amplifier. For the GSHE measurements the dc signal is sampled by an ADC, while for the ODMR method the signals are detected phase sensitive by a lock-in amplifier. As for GSHE phase-independent dc signals are recorded, the application of an analog low-pass filter (cutoff frequency: 90 Hz) helps to increase the signal-to-noise ratio when small signals are to be extracted (i.e., at low cell temperatures). The setup is enclosed by a threefold mu-metal shielding barrel leading to residual fields in the order of several nT, after careful demagnetization. The measurements were carried out fully automated and on average lasted about three working days for each cell.
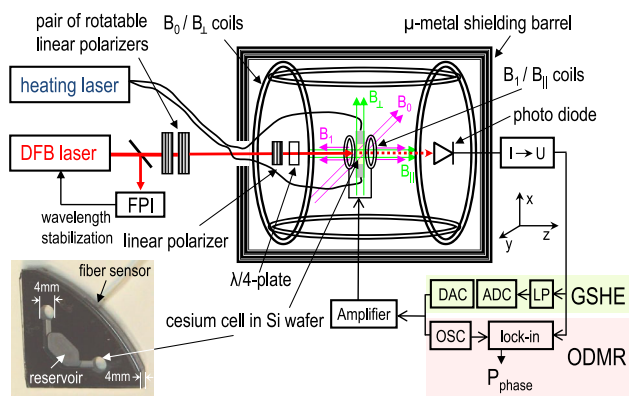
4 Results

The determination of γ_{20} using the ODMR method is demonstrated by Figs. 2 and 3: fitting (automatically symmetrized) phase curves, measured at different laser powers to (1) (Fig. 2) yields several values of γ_2. These are then used to extrapolate to vanishing laser power to obtain the intrinsic relaxation rate γ_{20} at different cell temperatures (Fig. 3).

The steps taken to confer the intrinsic relaxation rates using the GSHE method are demonstrated exemplarily for a single cell at a single temperature in Figs. 4–7: the Hanle resonances appearing in the transmitted laser power are recorded for different transversal magnetic field values, while sweeping the longitudinal field through zero (Fig. 4).
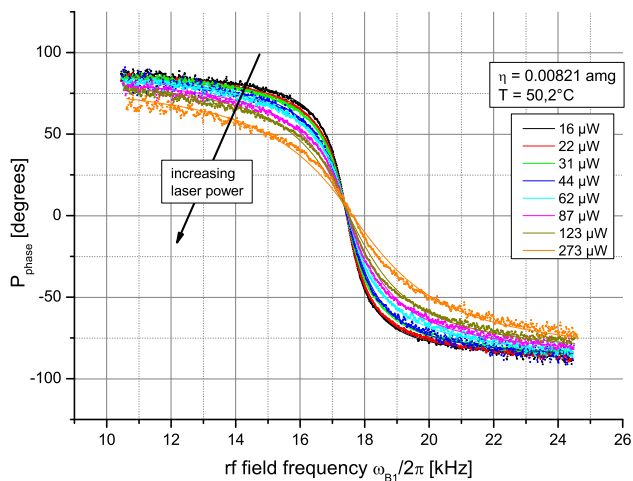

Fig. 1 Experimental setup. *FPI* Fabry-Perot interferometer, *OSC* oscillator, *DAC* digital-to-analog converter, *ADC* analog-to-digital converter, *LP* low-pass filter. *Inset* integrated vapor cell assembly

Fig. 2 Subset of ODMR phase signals (*dots*) recorded at $\eta = 0.00821$ amg and 50.2°C for several laser powers, fitted to (1) (*lines*)

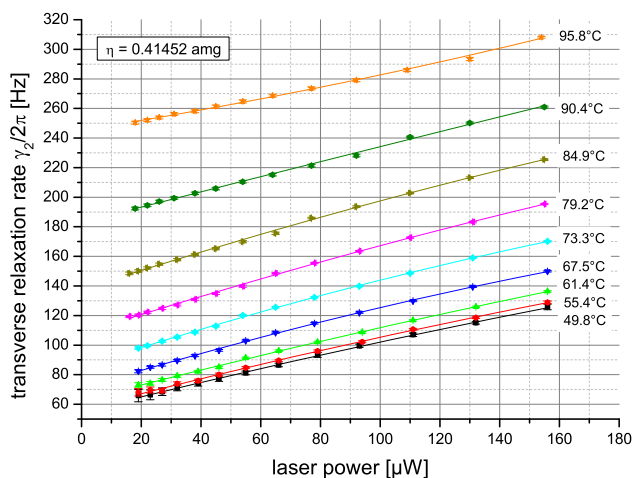**Fig. 3** ODMR measurements (*dots*, recorded at $\eta = 0.41452$ amg) and extrapolating fits (*lines*) to obtain intrinsic γ_{20} at zero laser power for several cell temperatures. Results at η different from the one in Fig. 2 are shown not for data quality reasons, but to have the best clearness in the example graphs

Fig. 4 LHE resonances as observed in detected photo current for sweeps of the longitudinal magnetic field through zero for different transverse magnetic field values for a single laser power (74 μW) and cell temperature (70.1°C) of the cell with $\eta = 0.106$ amg

Fig. 5 GSHE amplitudes (*squares*) and widths (*triangles*) extracted from preceding automatized Lorentzian fits to the data shown in Fig. 4 and subsequent fits (*lines*) to (4) and (5)

The amplitudes and widths of these resonances are inferred from automated Lorentzian fits. Their dependence on the transversal field value is fitted to (4) and (5) as shown in Fig. 5. The resulting parameters $P2 = \gamma_1\gamma_2$ and $P5 = \frac{\gamma_2}{\gamma_1}$ (Fig. 6) are then used in combination to derive the individual relaxation rates γ_1 and γ_2. Finally, extrapolation to vanishing laser power yields the intrinsic γ_{10} and γ_{20} (Fig. 7).

Unlike the results obtained by Castagna and Weis, with paraffin-coated room temperature vacuum cells, we observe an increasing ratio $\frac{\gamma_2}{\gamma_1}$ with increasing laser power in all GSHE measurements. In total, a different dependence of the relaxation rates on laser power results: At values where
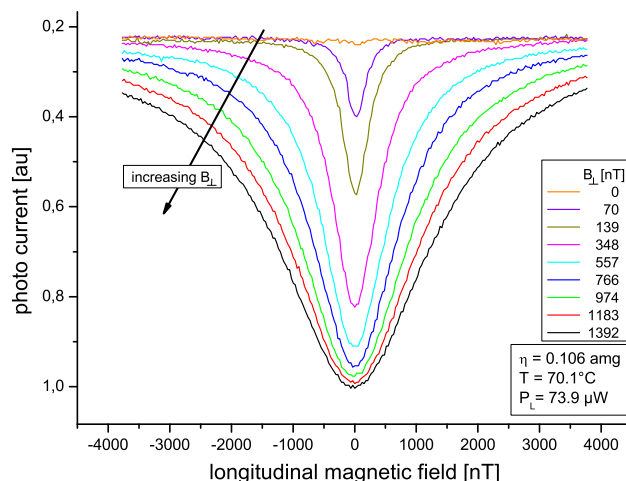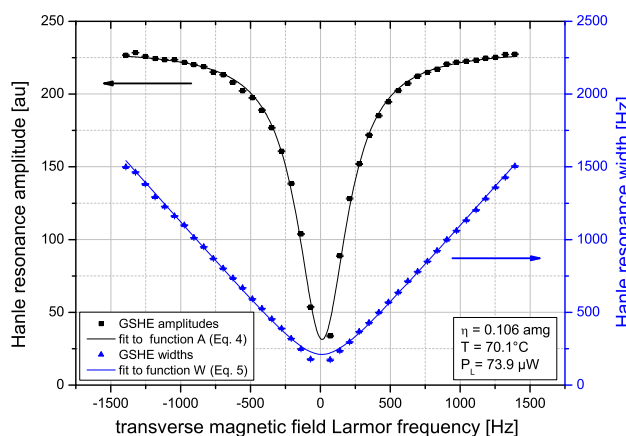
γ_2 still increases strongly, γ_1 already exhibits saturation behavior. To account for this, the proper data range of the empirical second-order polynomial extrapolation fits was set manually for every measurement run as we can not give a theoretic model yet (cf. Fig. 7).

The inferred intrinsic relaxation rates for the six cells filled with different nitrogen densities between 0.0082 amg and 0.414 amg using both methods are shown in Fig. 8 in dependence on cell temperatures between 40 and 120°C.

The ODMR result (Figs. 8a and b) shows the smallest linewidth at low temperature while, in accordance with (11), the linewidth strongly increases with rising cell temperature due to the spin-exchange contribution. Equation (11) is fitted to the data with every parameter fixed, only allowing variation due to an experimental offset in measured cell temperature ΔT that ranged up to 5°C. The
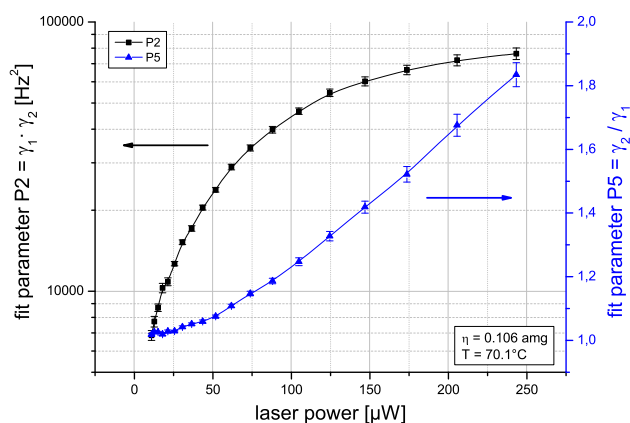
Fig. 6 GSHE fit parameters *P2* (*squares*) and *P5* (*triangles*) obtained from fits to (4) and (5) for the same η and cell temperature as shown in Figs. 4 and 5 in dependence on the laser power (please note the different y-scaling, *lines* are to guide the eye)
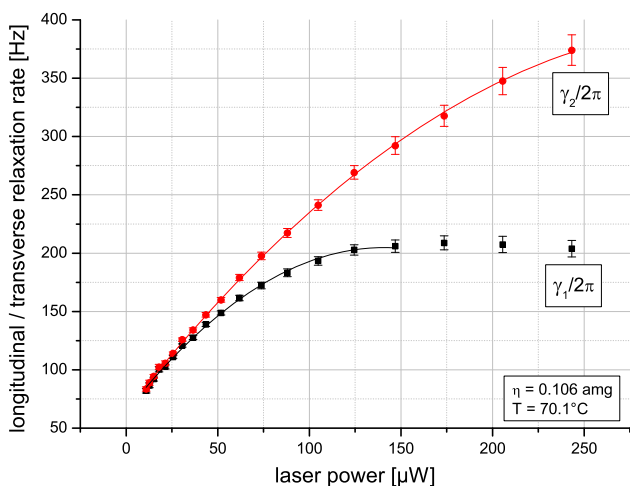

Fig. 7 GSHE values of γ_1 (*squares*) and γ_2 (*circles*) resulting from the parameters shown in Fig. 6 together with (phenomenological) second-order polynomial fits (*lines*)

data are well reproduced by the model equation, especially when the large number of (mostly experimentally determined) parameters taken from the literature is considered.

The GSHE result depicted in Figs. 8c and d shows only very weak temperature dependence what is explained by the vanishing spin-exchange contribution as discussed in Sect. 2.3. Consequently, for the GSHE data, (11) is plotted with fixed parameters again, but without the spin-exchange contribution R_{SE} [(i.e., (10)]. The experimentally determined intrinsic longitudinal and transverse relaxation rates are only slightly different. This is consistent with the intuitive expectation that the rates should be equal in the absence of any external laser and magnetic fields.

The GSHE data are in reasonable agreement with the model, but at high nitrogen pressures a deviation is apparent. The overall statistical quality of the GSHE data is inferior to that of the ODMR method, despite the fact that the both methods were conceded a similar amount of measurement time. The larger spread in the GSHE results might be attributed to an observed enhancement of the susceptibility to a laser frequency detuning compared with the ODMR method. This is yet to be studied in detail. Slow wandering of the laser frequency still occurred despite the active temperature stabilization of the FPI. Another source of statistical uncertainty may be attributed to the stronger nonlinear dependence on laser power the GSHE measurements show compared with the ODMR data, making the extrapolation to zero light power more delicate. Also, the more complex analysis procedure of the GSHE measurements may introduce a slightly pronounced statistical error. This in some way counteracts the advantage of less sophisticated experimental setup needed compared with the ODMR method based on

phase-sensitive detection.

For the analysis of the dependency on the nitrogen number density η the data are rearranged in Fig. 9 showing the measured intrinsic relaxation rates of the six cells at three temperatures along with the individual contributions of the relaxation processes according to (6–8).

The ODMR data is in nice agreement with the model. The inspection of the results in Fig. 9a at 50°C confirms the nitrogen pressure for minimum intrinsic linewidth to lie at about 0.2 amg for our cell geometry: At lower η wall relaxation is the dominant relaxation process, while increasing the pressure leads to the domination of the buffer gas induced depolarization. At higher cell temperatures for the ODMR method the spin-exchange broadening becomes dominant, while the intrinsic linewidth from GSHE measurements appears not to be limited by spin exchange. In principle, this finding enables the fast (approximate) determination of the cell-intrinsic relaxation rate constituted by the sum of the wall and buffer gas collision contributions at any given single cell temperature using the GSHE method. This might be useful for quick tests of newly developed wall coatings or buffer gas compositions. The exclusive occurrence of the spin-exchange relaxation in the ODMR method might also explain the discrepancy Castagna and Weis observed comparing their ODMR and GSHE measurements of γ_2 at room temperature [13, 22, 23]: The difference of 1.4 Hz between the measurements may in the main be attributed to the spin-exchange contribution of 1.2 Hz expected at 25°C according to (8).

While the GSHE measurements show good agreement with the model at low η, at high η the results suggest intrinsic linewidths to be below the limit set by buffer gas relaxation. For such a behavior, a plausible physical
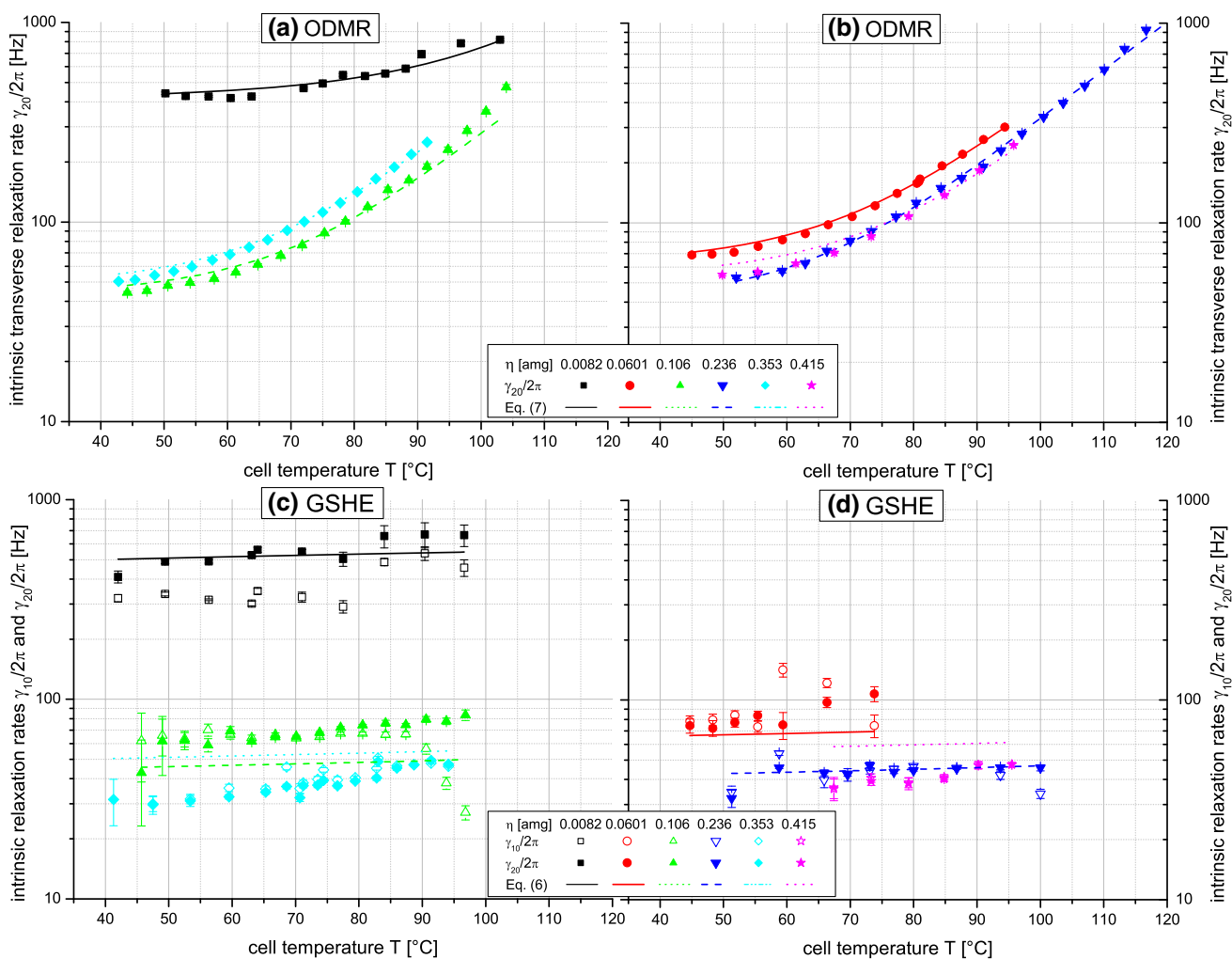
Fig. 8 Intrinsic transverse relaxation rates inferred using the ODMR method (**a** and **b**) and GSHE measurements (**c** and **d**). *Lines* represent fits to (11), for the GSHE model $R_{SE} = 0$ is set (see text for details). The nitrogen number density η is inferred from prior measurements of the Cs D_1 pressure line shift. *Error bars* shown reflect the uncertainties in the extrapolating fits to zero laser power. The results are shown in separate graphs for better visibility
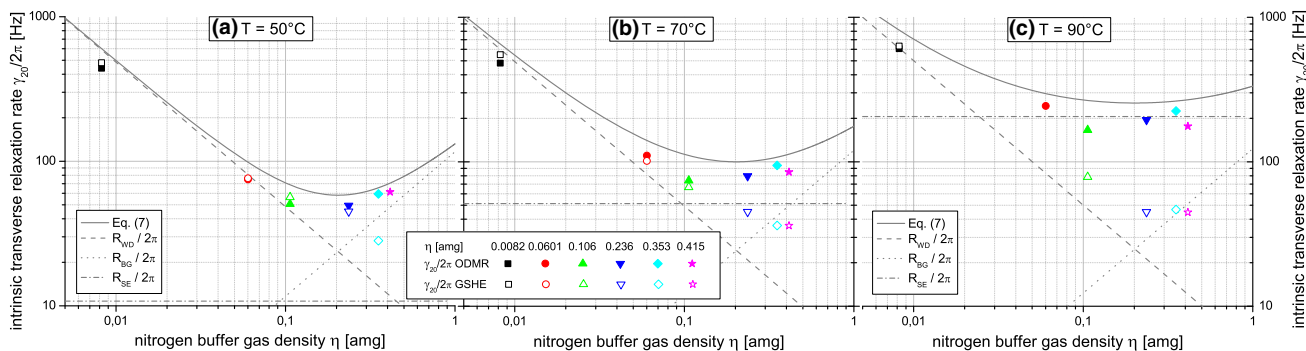

Fig. 9 Measured intrinsic relaxation rate γ_{20} for **a** low, **b** medium, and **c** high cell temperatures, inferred by interpolation of the ODMR data (*full symbols*) and GSHE results (*open symbols*). The *lines* represent models of the individual relaxation rates R_{WD}, R_{BG}, R_{SE} according to (6–8). Statistical *error bars* are below the dotsize

explanation does not exist. The problem here is found in the limited validity of (2–5); The model assumption made in [22, 23] of pumping only one single hyperfine transition

of the D_1 line gets slightly violated with growing η due to spectral pressure broadening and overlapping of the individual hyperfine transitions.

5 Conclusion

We have shown measurements of the intrinsic relaxation rates of miniaturized Cs cells using the ODMR and the GHSE method. As the measurements are carried out for a large range of temperatures and nitrogen buffer gas densities, the different contributing relaxation processes could be distinguished and their rate modeling confirmed. In contrast to the ODMR measurements, the GSHE results are insensitive to spin-exchange broadening leading to only very slight dependence on cell temperature for the whole range of our investigation. The results of both methods are in good agreement for low buffer gas pressures, where isolated hyperfine lines are encountered. At high buffer gas pressures, the GSHE results are questionable, as the model does not hold for pumping on broadened and overlapping hyperfine transitions without further elaborate extensions.

References

1. D. Budker, M. Romalis, Nat. Phys. **3**, 227 (2007). doi:10.1038/nphys566
2. E.B. Aleksandrov, A.K. Vershovskii, Phys. Usp. **52**, 573 (2009). doi:10.3367/UFNe.0179.200906f.0605
3. H.G. Dehmelt, Phys. Rev. **105**, 1924 (1957). doi:10.1103/PhysRev.105.1924
4. W.E. Bell, A.L. Bloom, Phys. Rev. **107**, 1559 (1957). doi:10.1103/PhysRev.107.1559
5. A.L. Bloom, Appl. Opt. **1**, 61 (1962). doi:10.1364/AO.1.000061
6. E.B. Alexandrov, M.V. Balabas, A.S. Pasgalev, A.K. Vershovskii, N.N. Yakobson, Laser Phys. 6, 244 (1996). http://www.antver.net/publ/articles/9en.pdf
7. S. Groeger, A.S. Pazgalev, A. Weis, Appl. Phys. B **80**, 645 (2005). doi:10.1007/s00340-005-1773-x
8. W.C. Griffith, S. Knappe, J. Kitching, Opt. Express **18**(26), 27167 (2010). doi:10.1364/OE.18.027167
9. H.B. Dang, A.C. Maloof, M.V. Romalis, Appl. Phys. Lett. **97**(15), 151110 (2010). doi:10.1063/1.3491215
10. W. Happer, Rev. Mod. Phys. **44**, 169 (1972). doi:10.1103/RevModPhys.44.169
11. H.G. Robinson, E.S. Ensberg, H.G. Dehmelt, Bull. Am. Phys. Soc. **3**, 9 (1958)
12. M.A. Bouchiat, J. Brossel, Phys. Rev. **147**, 41 (1966). doi:10.1103/PhysRev.147.41
13. N. Castagna, G. Bison, G. Di Domenico, A. Hofer, P. Knowles, C. Macchione, H. Saudan, A. Weis, Appl. Phys. B **96**, 763 (2009). doi:10.1007/s00340-009-3464-5
14. S.J. Seltzer, M.V. Romalis, J. Appl. Phys. **106**, 114905 (2009). doi:10.1063/1.3236649
15. M.V. Balabas, T. Karaulanov, M.P. Ledbetter, D. Budker, Phys. Rev. Lett. **105**, 070801 (2010). doi:10.1103/PhysRevLett.105.070801
16. N.D. Bhaskar, J. Pietras, J. Camparo, W. Happer, J. Liran, Phys. Rev. Lett. **44**, 930 (1980). doi:10.1103/PhysRevLett.44.930
17. W. Happer, H. Tang, Phys. Rev. Lett. **31**, 273 (1973). doi:10.1103/PhysRevLett.31.273
18. W. Happer, A.C. Tam, Phys. Rev. A **16**, 1877 (1977). doi:10.1103/PhysRevA.16.1877
19. J.C. Allred, R.N. Lyman, T.W. Kornack, M.V. Romalis, Phys. Rev. Lett. **89**, 130801 (2002). doi:10.1103/PhysRevLett.89.130801
20. I.K. Kominis, T.W. Kornack, J.C. Allred, M.V. Romalis, Nature **422**, 596 (2003). doi:10.1038/nature01484
21. E.B. Aleksandrov, M.V. Balabas, A.K. Vershovskii, A.E. Ivanov, N.N. Yakobson, V.L. Velichanskii, N.V. Senkov, Optika i Spectroskopiya **78**, 325 (1995)
22. N. Castagna, A. Weis, Phys. Rev. A **84**, 053421 (2011). doi:10.1103/PhysRevA.84.053421
23. N. Castagna, A. Weis, Phys. Rev. A **85**, 059907(E) (2012). doi:10.1103/PhysRevA.85.059907
24. S. Woetzel, V. Schultze, R. IJsselsteijn, T. Schulz, S. Anders, R. Stolz, H.G. Meyer, Rev. Sci. Instrum. **82**, 033111 (2011). doi:10.1063/1.3559304
25. T. Scholtes, V. Schultze, R. IJsselsteijn, S. Woetzel, H.G. Meyer, Phys. Rev. A **84**, 043416 (2011). doi:10.1103/PhysRevA.84.043416
26. T. Scholtes, V. Schultze, R. IJsselsteijn, S. Woetzel, H.G. Meyer, Phys. Rev. A **86**, 059904(E) (2012). doi:10.1103/PhysRevA.86.059904
27. G. Bison, R. Wynands, A. Weis, J. Opt. Soc. Am. B **22**, 77 (2005). doi:10.1364/JOSAB.22.000077
28. W. Hanle, Z. Phys. **30**, 93 (1924). doi:10.1007/BF01331827
29. G. Moruzzi, F. Strumia (eds.), *The Hanle Effect and Level-Crossing Spectroscopy* (Springer, 1991)
30. E.B. Alexandrov, *Interference of atomic states* (Springer, 1993)
31. J. Dupont-Roc, S. Haroche, C. Cohen-Tannoudji, Phys. Lett. A **28**(9), 638 (1969). doi:10.1016/0375-9601(69)90480-0
32. M. Bouchiat, J. Brossel, C. Cohen-Tannoudji, J. Dupont-Roc, S. Haroche, A. Kastler, J.C. Lehmann. Paramagnetic resonance and optical pumping magnetometer in the near zero magnetic field-range. Patent (1971). US 3629697 A
33. R.E. Slocum, Phys. Rev. Lett. **29**, 1642 (1972). doi:10.1103/PhysRevLett.29.1642
34. C. Andreeva, S. Cartaleva, Y. Dancheva, V. Biancalana, A. Burchianti, C. Marinelli, E. Mariotti, L. Moi, K. Nasyrov, Phys. Rev. A **66**, 012502 (2002). doi:10.1103/PhysRevA.66.012502
35. A. Huss, R. Lammegger, L. Windholz, E. Alipieva, S. Gateva, L. Petrov, E. Taskova, G. Todorov, J. Opt. Soc. Am. B **23**(9), 1729 (2006). doi:10.1364/JOSAB.23.001729
36. A. Vilardi, D. Tabarelli, L. Botti, A. Bertoldi, L. Ricci, J. Phys. B At. Mol. Opt. Phys. **42**(5), 055003 (2009). doi:10.1088/0953-4075/42/5/055003
37. H.J. Lee, H.S. Moon, J. Opt. Soc. Am. B **30**(8), 2301 (2013). doi:10.1364/JOSAB.30.002301
38. F.A. Franz, C. Volk, Phys. Rev. A **26**, 85 (1982). doi:10.1103/PhysRevA.26.85
39. S.J. Seltzer, Developments in alkali-metal atomic magnetometry. Ph.D. thesis, Princeton University (2008). http://physics.princeton.edu/romalis/papers/Seltzer%20Thesis.pdf
40. S. Appelt, A. Ben-Amar Baranga, C.J. Erickson, M.V. Romalis, A.R. Young, W. Happer, Phys. Rev. A **58**, 1412 (1998). doi:10.1103/PhysRevA.58.1412
41. T. Scholtes, V. Schultze, R. IJsselsteijn, S. Woetzel, H.G. Meyer, Opt. Express **20**, 29217 (2012). doi:10.1364/OE.20.029217
42. A.H. Couture, T.B. Clegg, B. Driehuys, J. Appl. Phys. **104**, 094912 (2008). doi:10.1063/1.3018181